Experimental study of concentrated particle transport in successively bifurcating vessels

Yinghui Li [1], Omid Amili [2], and Filippo Coletti [1,*]

[1]*Department of Mechanical and Process Engineering, Swiss Federal Institute of Technology (ETH), Zurich 8092, Switzerland*

[2]*Mechanical, Industrial, and Manufacturing Engineering Department, University of Toledo, Toledo, Ohio 43606, USA*

The flow features in branching networks are fundamental for the understanding of transport processes in respiratory and cardiovascular systems. Specifically for tumor embolization, the ability to predict the fate of finite-size particles in bifurcating vessels is highly desirable for improving embolization efficacy. Most past studies focused on very dilute regimes in which particles are not expected to interact with each other. In the present study, we use particle tracking velocimetry to investigate the spatial distribution, velocity, acceleration, and dispersion of finite-size particles in a four-generation bifurcating model. We consider a regime especially relevant to vascular embolization: a physiologic range of bulk flow Reynolds number and a suspension of neutrally buoyant particles with a diameter about 10 times smaller than the parent vessel diameter, reaching solid volume fractions up to 2%. We investigate how particles distribute among the distal branches and the influence of the release location. In addition, the effect of particle volume fraction is studied through Lagrangian statistics of the particle trajectories. Our results show the remarkable influence of particle concentration on particle transport in several ways. The particle traveling speed, acceleration, and dispersion are inhibited by the increasing particle volume fraction due to interparticle interactions. Importantly, the particles travel preferentially to the medial branches rather than to the lateral ones despite the uniform distribution of the distal volumetric flow rate. The findings provide insights relevant to the optimization of targeted drug delivery in embolization settings.

I. INTRODUCTION

With evolving imaging and computing technologies, the flow characteristics in successive bifurcating vessels have been widely investigated to understand the transport phenomena, for example, in blood vessels and pulmonary airways [1,2]. In particular, reaching a predictive understanding of particle transport through branching vessels is of great significance for biomedical applications including thrombo-embolization and drug delivery. Concerning specifically targeted tumor embolization (in which solid particles are aimed at the tumor to occlude its blood supply), the ability to predict particle behavior would be extremely beneficial in order to assist physicians in choosing the right particles and injection strategies to reach the target location within the intricate vasculature [3].

Previous studies have investigated the effects of different parameters on particles' fate. Bushi *et al.* examined the effect of the flow rate partition among the outlets and the particle-to-branch

---

*fcoletti@ethz.ch

diameter ratio on particle distribution in a simple bifurcation model [4]. The numerical study by Kennedy *et al.* [5] simulated microsphere transport in the hepatic arterial system and highlighted the influence of the inlet release location of the particles on their destination, as later validated experimentally by Richards *et al.* [6]. Basciano *et al.* [7], Zhu *et al.* [8], and Caine *et al.* [9] further demonstrated how particle trajectory and distribution are affected by particle density and diameter in the context of targeted embolization. The importance of particle properties and release location for the particle fate was also highlighted by Carr *et al.* [10] and Mukherjee *et al.* [11] in the context of cardiogenic and aortogenic emboli. Recently, Amili *et al.* [12] investigated the effect of flow Reynolds number and particle properties in the transport through successfully bifurcating vessels, demonstrating how the particle partition among the outlets can grossly depart from the volumetric flow partition, also emphasizing the link between the particles' release location and their fate.

In many settings including drug delivery, particle concentration is a crucial parameter due to, e.g., the need to deliver a sufficient amount of therapeutic agent to the target site. In the context of tumor embolization, high injection concentration is necessary to achieve efficient and complete vascular occlusion. At the fluid mechanic level, sufficiently dense concentrations can alter the underlying flow field and trigger consequential particle-particle interactions, affecting the transport process at multiple levels. Therefore, it appears essential to investigate how the particle volume fraction may affect their fate. To our best knowledge, however, the effect of concentration in suspensions through bifurcating vessels has been investigated only in the low Reynolds number limit relevant to blood microvasculatures (e.g., Ditchfield and Olbricht [13], and Stauber *et al.* [14]).

In the present study, we experimentally investigate the transport of sub-mm particles in a model network of successively bifurcating vessels under physiologically relevant conditions. We use high-speed imaging to reconstruct particles trajectories from the mother branch to the multiple distal outlets, observe how particles distribute among the distal branches, and focus on the unexplored effect of particle volume fraction. The paper is organized as follows: In Sec. II, we present the experimental apparatus, define the considered regimes, and describe the measurement techniques. In Sec. III, we present the results in terms of particle velocity, acceleration, pair dispersion, and distribution through the bifurcating vessels. In Sec. IV, we draw conclusions and give an outlook for future work.

II. METHODS

A. Experimental apparatus and flow regimes

We consider a successively branching tree of vessels (Fig. 1), in which the mother branch (G_0, diameter $D_0 = 8.6$ mm) bifurcates three times, in planar and symmetric fashion, into further branching generations (G_1 to G_3). The geometry follows the so-called Weibel model [15], which has been widely used in numerical and experimental studies relevant to both cardiovascular and respiratory flows (among others, Comer *et al.* [16], Jalal *et al.* [17], Chen *et al.* [18], and Amili *et al.* [12]). The geometry consists of repetitive self-similar branching units, with a child-to-parent diameter ratio $D_{i+1}/D_i = 0.7$, a branch length-to-diameter ratio $L_i/D_i = 3.5$ (except for G_0, which is significantly longer to allow for fully developed inflow conditions), and a bifurcation angle of $60°$. We define a coordinate system in which the x-y plane coincides with the plane of the bifurcation. The x axis is aligned with the centerline of G_0, such that both x-y and y-z are symmetry planes of the geometry. We place the origin at a distance $5D_0$ from the first bifurcation's carina, approximately coinciding with the beginning of the region investigated via imaging.

The model is three-dimensional (3D) printed out of a clear resin (Somos WaterShed XC 11122) by high-resolution stereolithography at the W. M. Keck Center (University of Texas at El Paso, TX). The printing layer thickness of 50 μm, the wall thickness of 0.3 mm, and the chemically polished surfaces guarantee hydrodynamically smooth walls and minimal optical distortion. The latter is further reduced by imaging the model through a water-filled enclosure, 3D printed in one piece with the bifurcation and sealed by 3-mm-thick acrylic plates.

TABLE I. Summary of the nondimensional parameters for the investigated cases.

Re	St	ϕ_V
750	0.156	0.4%
750	0.156	2%
1500	0.312	0.2%
1500	0.312	1%
1500	0.312	2%

The flow loop is depicted in Fig. 2. The model inlet is connected to a 3D-printed cylindrical tube of the same diameter as G_0 and length of 250 mm ($30D_0$). The working fluid is water, circulated by a 5-MD-SC Little Giant centrifugal pump from a holding tank through stainless steel tubing. The flow rate imposed by the pump is monitored by an Atrato 760-V-1-0-SD ultrasonic flow meter. A water-particle suspension of known concentration, delivered by a syringe pump (Chemyx Fusion 200) at a flow rate of 120 mL/min, is added to the main water flow through a T-junction located at approximately $60D_0$ upstream of the bifurcation model. The particles are neutrally buoyant fluorescent polyethylene beads (Cospheric LLC) with a density of $\rho_p = 1000$ kg/m$^3 \pm 1\%$ and a diameter of $D_p = 425$–500 μm. Each of the eight distal branch (G_3) is connected to a 1.5-m-long plastic tubing, 6.4 mm in diameter, which imposes the same flow resistance to all outlets. This ensures that the flow rate is equally distributed among all branches, as verified by monitoring each outflow by a ME-6PXL Transonic clamp-on flow meter with an absolute accuracy of $\pm10\%$ of the reading. Each tubing returns the water to the holding tank, which is equipped with a 300-μm filtering net, ensuring clear water delivered by the pump and a constant particle volume fraction in the model. The latter is adjusted by changing the volume fraction in the syringe between approximately 1% and 10%, which, depending on the water flow rate, leads to a range of volume fractions in the bifurcation, $\phi_V = 0.1\%$–2%. At the higher concentrations, the mean interparticle distance (assuming homogeneous spatial distribution) is just $3D_p$ and the particles are expected to significantly affect the fluid flow and each other's motion. Therefore, particle-particle interaction is expected to play a major role, though in the form of binary collisions rather than sustained particle-particle contact [19].
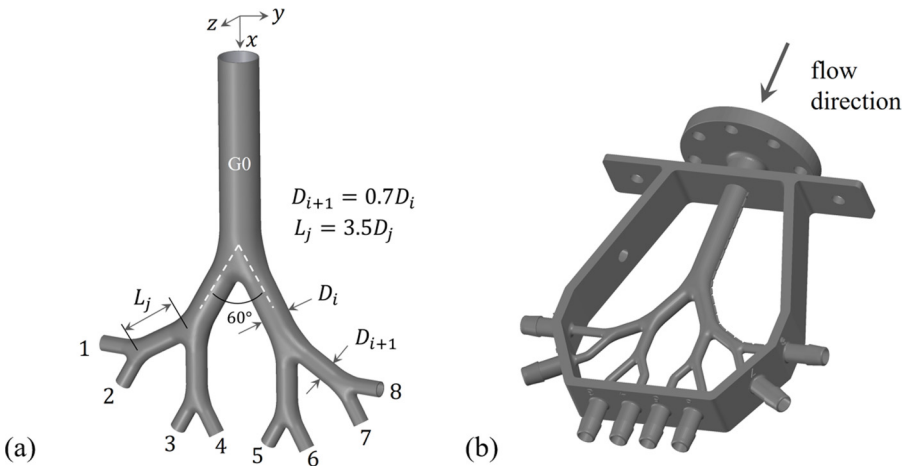

FIG. 1. (a) Geometry of idealized bifurcation and (b) 3D-printed model with enclosure and lateral marks along the center plane for imaging focusing.
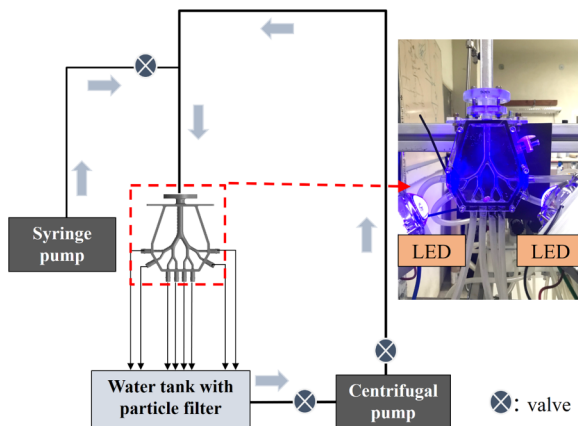
FIG. 2. Schematic of the experimental setup for particle imaging with an enlarged view of the LED-illuminated model.

The main experimental parameters for the investigated cases are summarized in Table I. The range of Reynolds number (Re) defined at the mother branch, $Re = U_0 D_0/\nu = 750, 1500$ (where U_0 is the bulk flow velocity at G_0, and ν is the kinematic viscosity of water), is relevant to an array of physiological flows, in particular the main hepatic artery where a steady flow assumption is often made [5,7]. The particle Stokes number, $St = \tau_p/t_0$, compares the particle response time $\tau_p = \rho_p D_p^2/(18\mu)$ (where μ is the dynamic viscosity of water) to the characteristic timescale of the inflow, $t_0 = D_0/U_0$. The present St range indicates significant inertia of the particles, and thus possibly large departures of their trajectories from the fluid path lines.

B. Measurement approach

The particle motion is captured by a 4-Megapixel Phantom VEO 640L high-speed camera mounting a 200 mm MicroNikkor lens to give a resolution of 54 μm/pixel. Fiducial marks 3D printed on the external walls of the bifurcation, as shown in Fig. 1(b), enable accurate focusing on the x-y plane. The camera is operated at 350 Hz for $Re = 1500$ and 200 Hz for $Re = 750$, keeping the frame-to-frame particle displacement within 15 pixels (about 1.6 particle diameter). Approximately 3000 and 5000 images are acquired over 10 seconds (equivalent to approximately 10 times the through-flow time at $Re = 750$) for the higher and lower Re, respectively. Front illumination is provided by two 100-W blue LEDs with a wavelength of 460–470 nm. A narrow-band-pass filter at 520 nm is attached to the lens to ensure that only the green light scattered from the fluorescent particles is captured by the camera. As mentioned, light distortion is negligible, as indicated by imaging optical targets through the water-filled enclosure, and by the fact that the particle images remain round at all locations. Figure 3 shows sample snapshots at increasing volume fractions. Particle centroids are found by a circle-finder algorithm and the trajectories are computed via an in-house particle tracking velocimetry (PTV) code based on the four-frame best estimate method proposed by Ouellette *et al.* [20]. The particle velocities and accelerations are obtained by convolving the trajectories with the derivative of a Gaussian kernel in the time domain. The size of the kernel is chosen as the value beyond which the acceleration variance decays exponentially, as in several previous particle-laden flow studies [21–23].

With a lens aperture f/4, the depth of focus is calculated to be approximately 1.2 mm. As the volume fraction increases, the number of out-of-focus particles in front of and behind the focal plane increases, especially in the larger mother branch. To avoid tracking them, we leverage the fact that these are farther from the vessel centerline and therefore travel slower. Thus, we disregard particles having velocities smaller than 50% of the local mean within a window of 12×12 pixels;

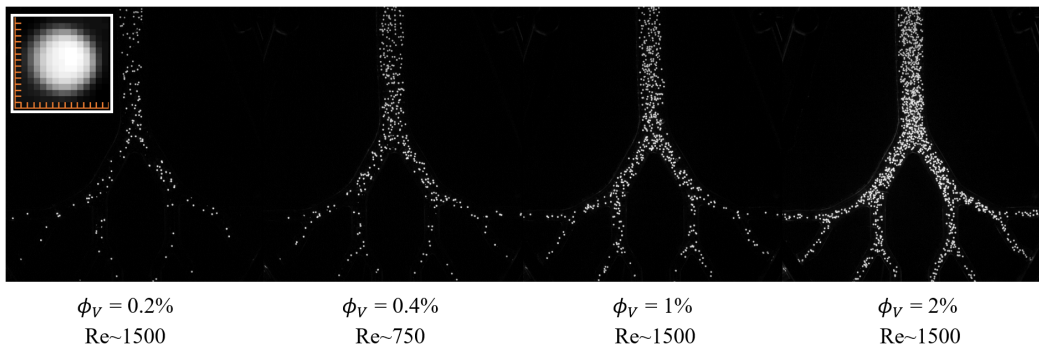| $\phi_V = 0.2\%$	$\phi_V = 0.4\%$	$\phi_V = 1\%$	$\phi_V = 2\%$
Re~1500	Re~750	Re~1500	Re~1500

FIG. 3. Four snapshot images at the four increasing particle concentrations considered with enlarged particle image and pixel size shown on the upper left.

the reported results are only weakly sensitive to the precise value of such threshold. While the present imaging approach complicates the task of accurately locating the particles in the depth (z) direction, it enables tracking much longer trajectories compared to illuminating a slice of the domain with a light sheet.

To characterize the baseline flow, particle image velocimetry (PIV) is performed on the unladen water. Neutrally buoyant polyethylene tracers [20–27 μm in diameter, St $= O(10^{-4})$] are imaged at 700 and 350 Hz at the higher and lower Re, respectively, collecting 3000 frames for each run. Velocity vectors are computed using a standard cross-correlation algorithm, with an initial interrogation window of 48×48 pixels, refined to 24×24 pixels and 50% overlap, for a final vector spacing of 0.65 mm.

The uncertainty in the PTV results derives from bias errors due to incorrect particle location or tracking, and from random errors due to the finite sample size. The bias errors are estimated by tracking sets of synthetic particles generated from the actual images, similar to [23]. As the centroid location is determined with subpixel accuracy (compared to the particle diameter of 10 pixels), the particle location errors are negligible. Tracking errors are also not significant as the tracked particles are typically at a larger distance from each other compared to the search radius [20]. The random errors amount to an uncertainty within $0.1U_0$ for the mean particle velocity field, based on a 95% confidence interval [24].

III. RESULTS

A. Particle velocity and acceleration

To characterize the time-averaged particle behavior, the PTV data are binned in windows of 0.65×0.65 mm, matching the final interrogation window size of the PIV measurements of the unladen fluid. In order to define inlet conditions, Fig. 4 shows mean radial profiles of particle velocity normalized by U_0 and particle concentration for the cases of Re $= 1500$ in the G_0 region, averaged in the region $0 < x < 2.5D_0$. Here and in the following, selected cases are shown to illustrate the trends, implying those are maintained in all cases. The velocity profiles display an approximately parabolic profile, though with significant velocities of the near-wall particles. Thus the latter move significantly faster than the local fluid, which obeys the no-slip boundary condition at the wall. At the highest ϕ_V, the velocity profile becomes somewhat flatter. Such flattening is visible also in the concentration profiles, which tend towards a top-hat shape as the volume fraction increases. We note that the inlet profiles of velocity and concentration display a degree of asymmetry which becomes visible at the higher concentration. This is likely associated to the T-junction where the water-particle suspension meets the main water flow, as described before. The asymmetry is
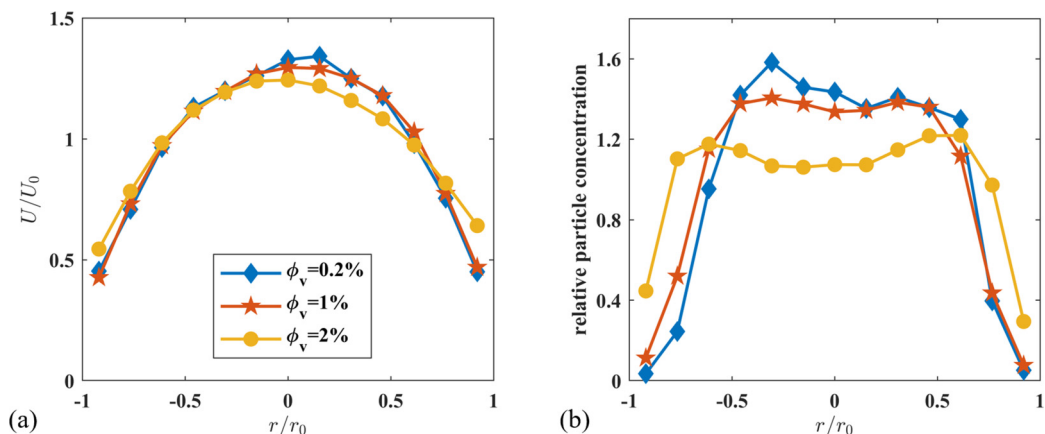
FIG. 4. (a) Inlet particle velocity profile normalized by the fluid bulk velocity (U_0) across the radius of G_0 (r_0), and (b) relative particle concentration profile for the Re = 1500 cases.

largely but not completely dissipated by the long development length. However, as the asymmetry amounts to less than 10%, it is not believed to be influential for the reported trends.

Figure 5 compares the time-averaged fields of the velocity magnitude $|U|$ (along the x-y imaging plane) for the fluid and the particles at the different considered ϕ_V and Re, normalized by U_0. The fluid flow (shown for Re = 750, quantitatively similar to the Re = 1500 case) displays the pattern expected from previous studies, including relatively large velocities along the inner side of the G_1 branches and significant deceleration at the carinas [16,17]. Both of these features are also apparent, and in fact accentuated, in the particle fields; especially at the higher concentrations, the velocity is vanishingly small at the carinas where the inertial particles collide with the wall. In general, the speed of the particles at the lower concentrations is close to that of the unladen fluid, but decreases with increasing ϕ_V, likely due to more frequent collisions dissipating kinetic energy. This is evident in Fig. 6, where the cross-sectional average velocity of the particles at the main branch, U_{0p}, is plotted as a function of ϕ_V, showing a decreasing trend.

To further explore the influence of volume fraction on the particle motion, the Lagrangian velocity autocorrelation ρ_u of the particle velocity fluctuations in G_0 ($0 < x < 4D_0$) is calculated as a function of the time lag t:

$$\rho_u(t) = \left\langle \frac{(u_{t0} - U_{t0,x})(u_{t0+t} - U_{t0+t,x})}{\sigma^2} \right\rangle. \tag{1}$$

Here, u_{t0} is the instantaneous particle velocity at the initial time t_0, from which we subtract the local time-averaged velocity $U_{t0,x}$. The latter is obtained by linearly interpolating the mean velocity fields (as shown in Fig. 5) at the instantaneous particle location. Angle brackets denote ensemble averaging. The velocity variance σ^2 is calculated as

$$\sigma^2 = \overline{(u_{t0} - U_{t0,x})^2}, \tag{2}$$

where the overbar denotes averaging along the particle trajectory. To avoid spatial inhomogeneity in the near-wall regions, we only consider trajectories in the core of G_0 (conventionally defined by a radial distance $r < D_0/4$ from the vessel axis); including all radial locations yields analogous conclusions. As shown in Fig. 7 for the cases at Re = 1500, the velocity autocorrelation for the lower volume fraction barely decays over time, as in a laminar steady flow. The hypothesis of flow laminarity in this regime is supported by the limited Reynolds number and the highly dilute suspension, but it cannot be strictly verified here, as the flow is not directly imaged using tracers. The decay is faster with increasing volume fraction, and for the higher concentration
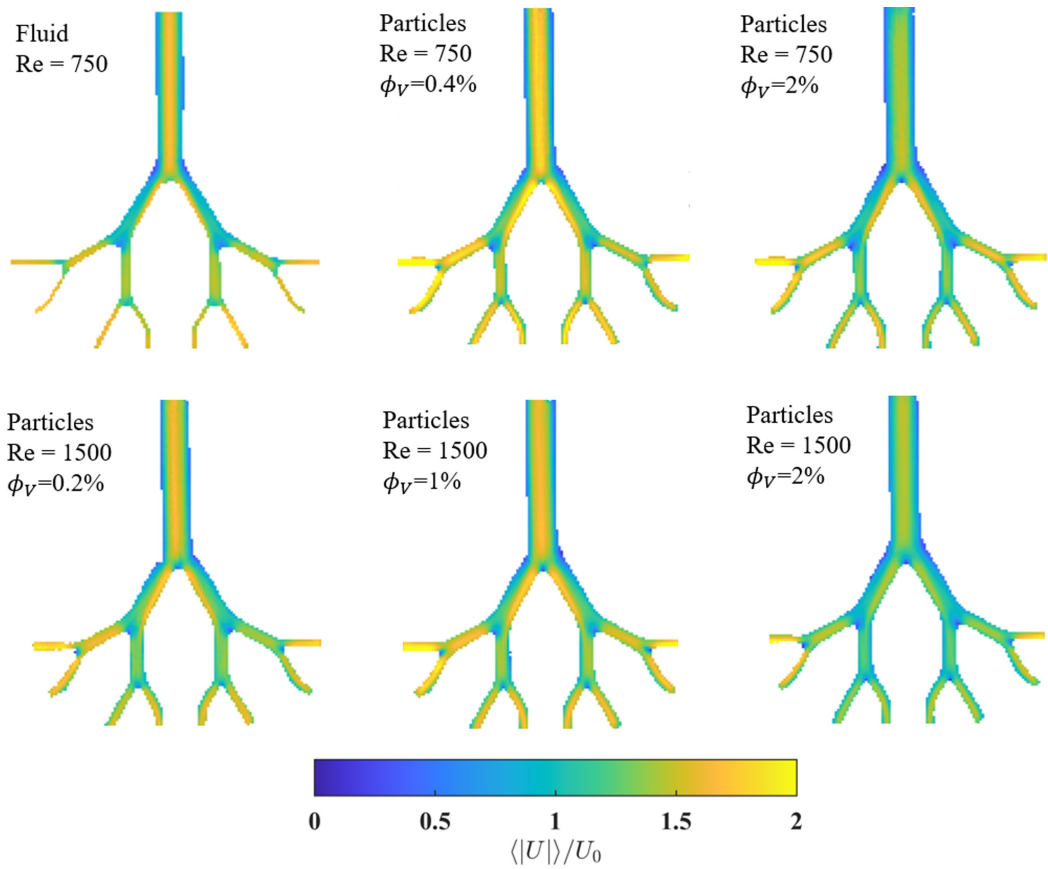
FIG. 5. Time-averaged fields of the velocity magnitude $|U|$ for the fluid and the particles at the different considered ϕ_V and Re, normalized by the bulk velocity of the fluid.
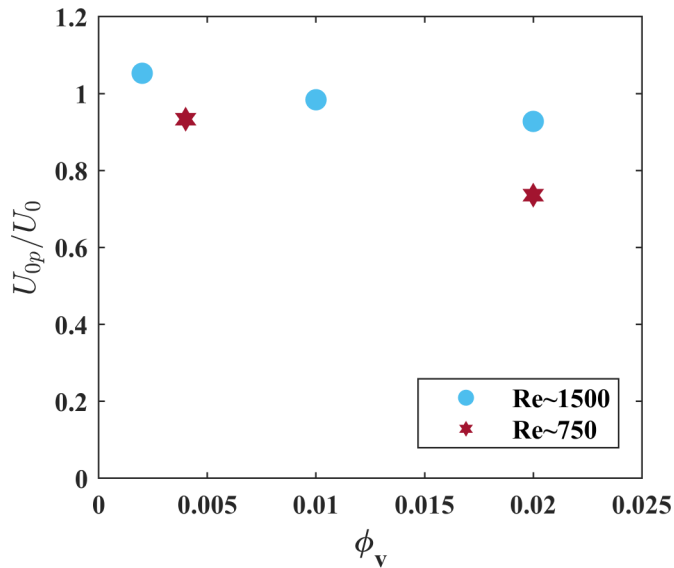

FIG. 6. Bulk velocity of particles of the different cases, normalized by the bulk velocity of the fluid.
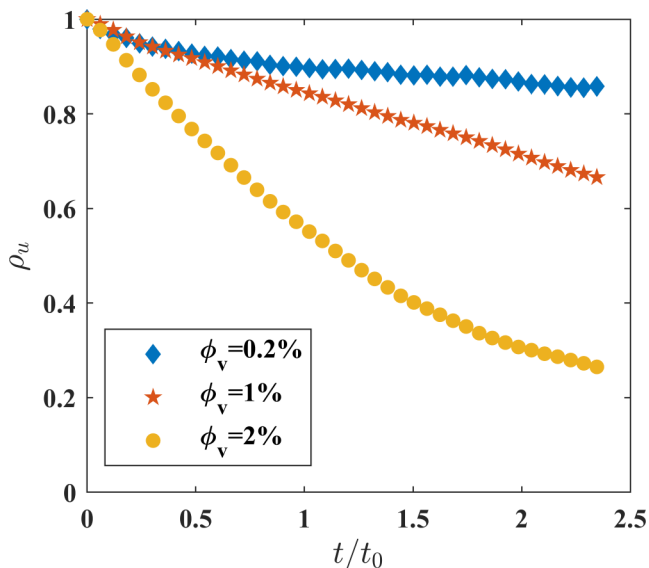
FIG. 7. Lagrangian autocorrelation of the particle velocity fluctuations in the mother branch G_0 at Re = 1500.

the signal decorrelates over a timescale comparable to t_0. In particular, at $\phi_V = 2\%$, the velocity autocorrelation decays exponentially and reaches an e-fold drop in a time delay of approximately $1.5t_0$. This suggest that in the denser regimes, frequent interparticle interactions cause the particle to gradually lose memory of its previous state. At the considered volume fractions, however, the motion is far from Brownian and the velocity fluctuations remain correlated over timescales characteristic of the underlying fluid flow.

The particle-particle and wall-particle interactions lead to locally large accelerations, as demonstrated by the probability density functions (PDFs) of the acceleration magnitude. These are plotted in Fig. 8(a), normalized by the respective root-mean-square (rms) values. The cases shown have a
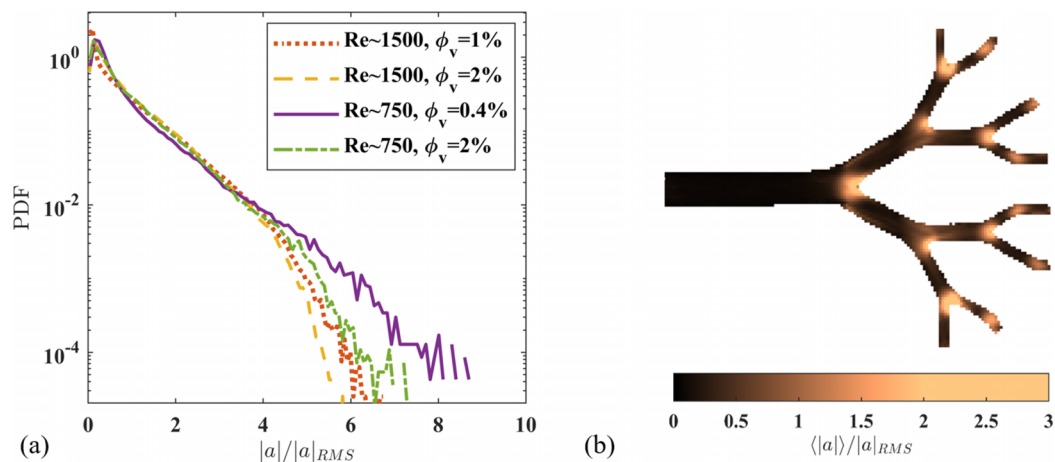

FIG. 8. (a) PDF of acceleration magnitude $|a|$ normalized by the respective rms acceleration for selected cases. (b) Time-averaged field of normalized acceleration for the case Re = 1500, $\phi_V = 1\%$.
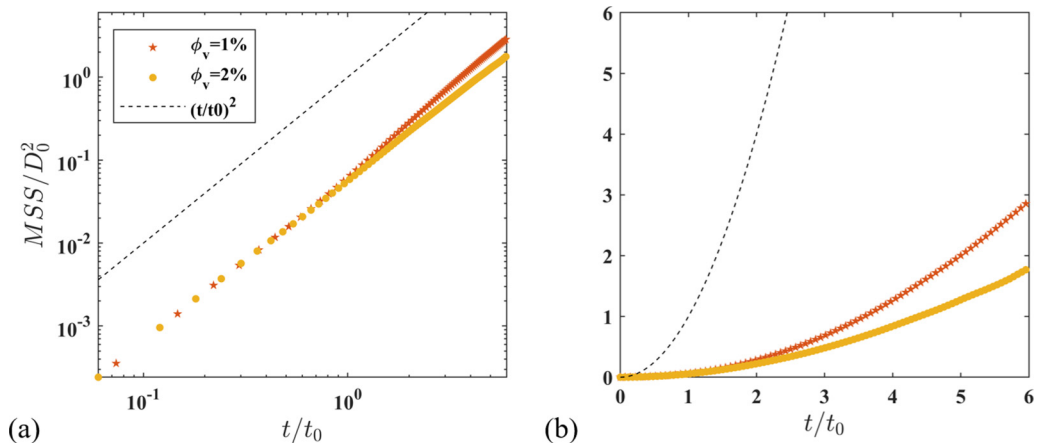
FIG. 9. Unconditioned mean-square separation at different volume fractions for the case Re = 1500 plotted with (a) logarithmic axes and (b) linear axes.

sufficient number of measured trajectories to describe this quantity, the distributions being largely unaffected if half of the samples are randomly removed. The PDFs possess long exponential tails characteristic of an intermittent process, similar to the accelerations of small particles in turbulent flows [25]. The spatial maps of the acceleration magnitude confirm that most of the extreme events are concentrated in the bifurcation regions, where particles collide with the carina. This is shown in Fig. 8(b) for the case Re = 1500 and $\phi_V = 1\%$, with all other cases displaying equivalent spatial distributions.

B. Particle dispersion

We then investigate how the volume fraction affects the dispersion of the particles through the bifurcating vessels. This is quantified through the mean-square separation (MSS) of particle pairs as a function of time t,

$$\text{MSS}(t) = \langle (d(t) - d_0)^2 \rangle, \tag{3}$$

where particles are paired with their neighbors with an initial distance $d_0 < 0.25D_0$, and $d(t)$ is the distance between particle pairs, to which we subtract the initial separation d_0 to account for the possible correlation between initial separation and relative velocity of the pair [26]. By limiting the initial separation to $0.25D_0$, we aim to isolate the dispersion due to particle-fluid dynamics, as opposed to the separation imposed by the geometric bifurcation (which is addressed later). Relatively small changes of such threshold do not affect the conclusions. The unconditioned MSS (considering all particle pairs) is presented in Fig. 9 for the Re = 1500 case, comparing ϕ_V = 1% and 2% in both linear and logarithmic axes. At $\phi_V = 1\%$, the t^2 scaling [clearly visible with logarithmic axes in Fig. 9(a)] indicates a ballistic regime, i.e., particle separations increasing approximately linearly with time. At $\phi_V = 2\%$, however, there is a significant reduction in the growth rate of MSS at long times, as apparent with linear axes in Fig. 9(b). This suggests that the particle relative movement is hindered by the increased concentration, i.e., the particles obstruct each other's motion and thus slow down the relative dispersion process.

The trend is confirmed by investigating the trajectory-wise mean-square separation, MSS_{traj}: this is calculated considering particles in the upstream region of $G_0(0 < x < 2D_0)$, pairing each one with its neighbors with an initial separation $d_0 < 0.25D_0$ and tracking their separation over time. This observable, shown in Fig. 10(a) for the same cases as Fig. 9, allows us to evaluate how particle pairs separate from each other along a temporal abscissa with a specified origin: $t = 0$ corresponds
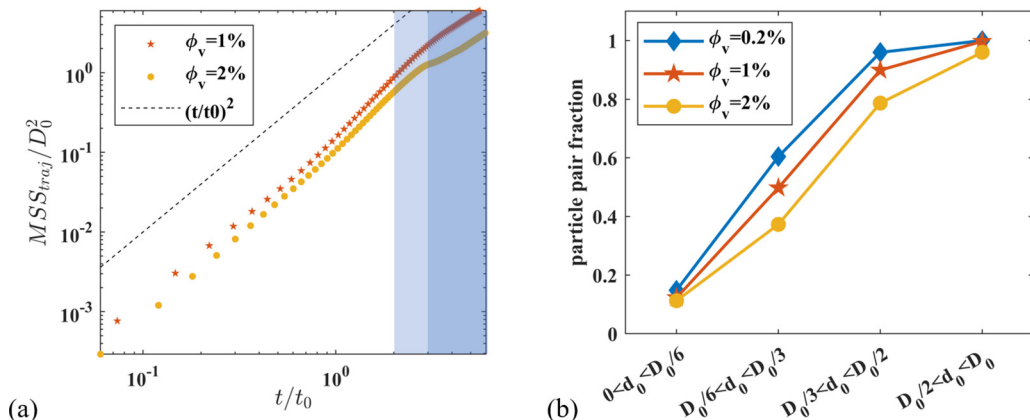
FIG. 10. (a) Trajectory-wise MSS as a function of time, with the time range when particles approximately enter G_1 and G_2 colored in light blue and deep blue, respectively. (b) The fraction of separated particle pairs (at the first bifurcation) grouped in different ranges of initial radial distance.

to the beginning of the imaged part of G_0. The separation is ballistic at first (up to $t/t_0 \sim 1$), then the MSS gradually accelerates as the particles enter the first bifurcation and some pairs break apart ($t/t_0 \sim 2$). When entering the narrower G_1, however, the particles are confined to remain relatively close to each other, and their MSS grows more slowly ($t/t_0 \sim 3$). This contrasts with the intuitive notion that a bifurcating tree would enhance spatial spreading of the particles. Such change in trend is significantly sharper for the larger ϕ_V, confirming that the higher particle concentration inhibits the dispersion process. Indeed, by the time they exit G_3, the initially nearby particles are separated by almost $3D_0$ in the $\phi_V = 1\%$ case and $\sim 2D_0$ in the $\phi_V = 2\%$ case. The probability of particle pairs in the mother branch to separate when entering the first bifurcation is quantified in Fig. 10(b), as a function of their initial separation d_0 (projected in the radial direction of G_0). This plot confirms that for the same range of initial separations, the probability that particle pairs break apart at the bifurcation decreases significantly with increasing concentration.

C. Particle partition among distal branches

We finally analyze how the particles distribute among the outlet branches of the vessel tree. Because the bifurcation model is symmetric and each of the outlets receives an equal flow rate, one may expect the particles to also distribute evenly. Recent studies show, however, that this expectation is misplaced: in a similar geometry and Re regime (though with less inertial particles and much more dilute concentration), Amili *et al.* [12] found large differences in the fraction of particles that reaches adjacent distal branches, largely departing from the volumetric flow rate partition. This counterintuitive behavior is partly rooted in the nonsymmetric distribution of the fluid momentum. Indeed, Jalal *et al.* [17] showed that the skewed fluid velocity profile in G_1 (as seen in Fig. 5) leads to a larger mass flow rate in the medial than in the lateral G_2 branches when all are kept at the same outlet pressure. We also note that in respiratory flow simulations of particle transport in the bronchial tree, the medial branches were found to be favored using both Euler-Euler and Euler-Lagrange simulations [27,28]. Here these effects are compounded with those of particle inertia (which limits the particle ability to follow curving streamlines) and concentration (which hinders the dispersion, as seen above). Figure 11 displays the fraction of particles that reaches the different outlet branches for both Re = 1500 and Re = 750, averaging between both symmetric halves of the model. The particles clearly favor the middle branches over the lateral ones, despite all outlets receiving the same fluid flow rate. The effect appears rather independent of the volume fraction.
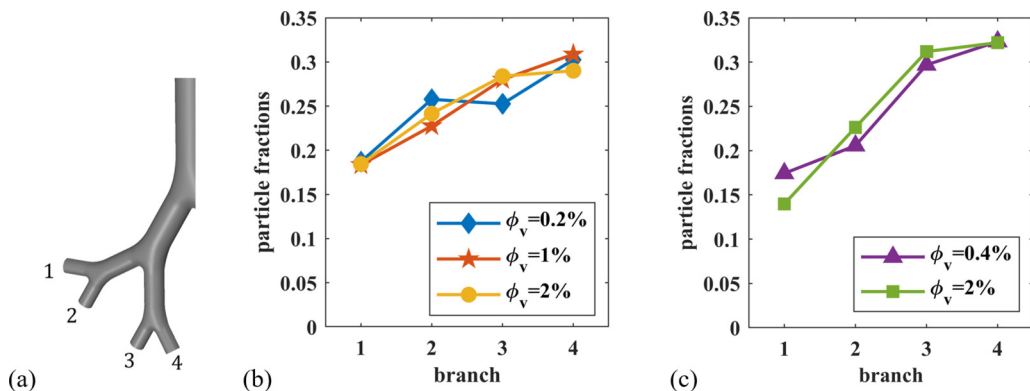
FIG. 11. (a) Numbering of the distal branches. Distribution of particles among distal branches for (b) Re = 1500 and (c) Re = 750.

The role of the volume fraction is instead clearly highlighted by inspecting the origin of the particles that reach the different outlet branches. Kleinstreuer and collaborators [5,7] and Amili *et al.* [12] demonstrated that the release position of the particles in the mother branch crucially impacts their destination several bifurcations downstream. Here we distinguish between particles originating from the core and the periphery of the G_0 cross section, again defined by having an initial radial location r smaller and larger than $D_0/4$, respectively. Figure 12 reports the fraction of the particles reaching the different outlet branches for the Re = 1500 case, for different ϕ_V. At $\phi_V = 0.2\%$, regardless of the destination branch, most of the tracked particles originate from the core region. With increasing concentration, however, the fraction originating from the peripheral region increases significantly, as the particles distribute more homogeneously over the cross section of the mother branch [see Fig. 4(b)]. Remarkably, while the fraction originating from the core remains predominant among the particles reaching the medial branches, with increasing ϕ_V the lateral branches receive more and more particles from the periphery of G_0. This trend is consistent with the fundamental observation made above, that more concentrated particles tend to disperse less. As such, in the dense regimes, particles released close to the wall of the mother branch experience less lateral migration compared to the more dilute case, and thus are more likely to reach the lateral branches.

IV. CONCLUSIONS

We have investigated the transport of inertial particles in successively bifurcating vessels. The geometry, flow regimes, and particle properties in terms of density (compared to the fluid) and size (compared to the vessel diameter) are relevant to a wealth of physiological and biomedical settings, in particular the embolization of the hepatic circulation [1,3,5,7,29]. Considering volume fractions between 0.2% and 2%, we focus on the role of particle concentration.

While the particle velocity fields qualitatively resemble that of the unladen fluid, the velocity of the suspended phase decreases with increasing concentration. This is interpreted as a consequence of particle-particle interactions and particle-wall collision, especially at the carina. The latter results in large and intermittent particle accelerations, which may be important to consider when modeling the transport using the stochastic model [30]. The interparticle interactions also cause a loss of memory along the particle trajectories, whose velocity fluctuations remain, however, correlated over the characteristic timescales of the flows. Over the considered range of volume fractions, the dispersion process is hindered at increasing concentrations, as the particles obstruct each other's lateral motion. The surprising consequence is that already for volume fractions of only 1%, particle pairs separate, on average, less quickly through the bed of bifurcating vessels than they do within the mother branch. Despite the volumetric flow rate being uniformly partitioned among the distal branches,
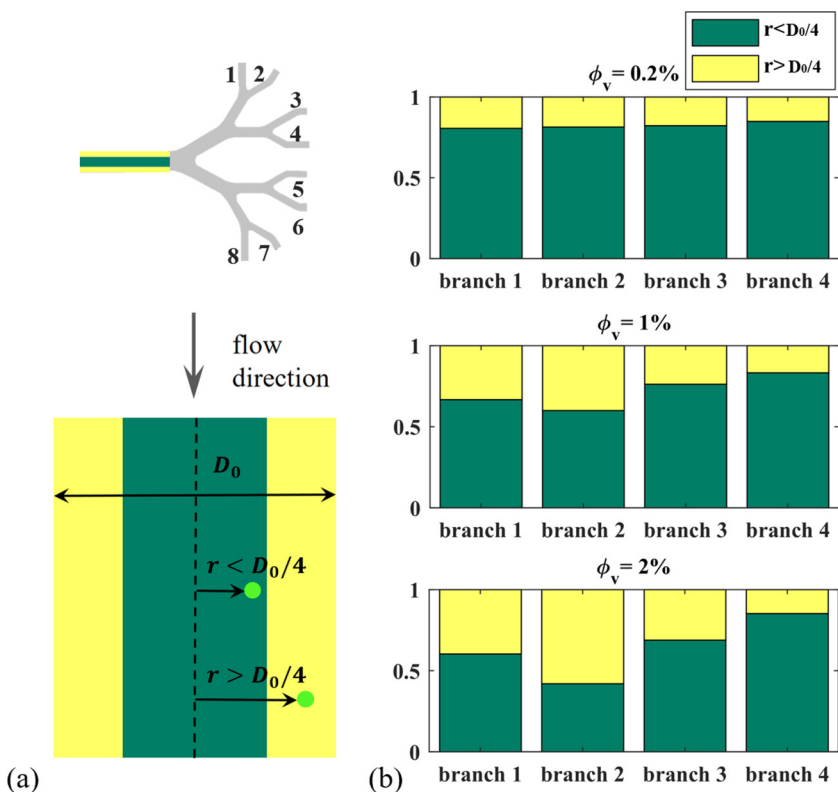
FIG. 12. (a) The center plane of G_0 is divided into two regions: the core (green) and the periphery (yellow). (b) Bar chart showing the fractions of particles originating from the core region and periphery of G_0 and reaching each distal branch.

the inertial particles travel preferentially to the medial branches rather than to the lateral ones. The reduced particle dispersion at the higher concentration translates into a stronger correlation between the distal branch of destination and the particle position several bifurcations upstream: at relatively large volume fractions, the majority of the particles reaching the medial or lateral branches originate from the core or peripheral region of the mother branch, respectively. This suggests that more concentrated suspensions may facilitate the targeting of specific vessels. Such a consideration is especially important for drug delivery, as typically catheters can only reach far upstream of the target location in the vasculature; and in particular for release strategies that optimize the injection location based on the underlying fluid flow [31,32].

The present work focuses on one particle type, and as such the Stokes number varies with the flow Reynolds number. Further studies investigating different particle types are warranted to disentangle the effect of St and Re, and to explore larger particle-to-vessel diameter ratios; the latter will likely lead to a stronger two-way coupling between the continuous and dispersed phases. We remark that higher volume fractions than those considered here would also be of interest, but they would require either different measurement techniques or the use of a quasi-two-dimensional geometry. Moreover, we deliberately considered an idealized geometry in order to isolate fundamental aspects of the particle-fluid dynamics problem. Future studies shall consider configurations relevant to specific anatomical sites, as well as pulsatile flow regimes and compliant walls that would increase the realism towards biomedical applications.

---

[1] C. Kleinstreuer and Z. Zhang, Airflow and particle transport in the human respiratory system, Annu. Rev. Fluid Mech. **42**, 301 (2010).

[2] T. W. Secomb, Blood flow in the microcirculation, Annu. Rev. Fluid Mech. **49**, 443 (2017).

[3] J. Hartke, M. Johnson, and M. Ghabril, The diagnosis and treatment of hepatocellular carcinoma, in *Seminars in Diagnostic Pathology* (Elsevier, New York, 2017), Vol. 34, pp. 153–159.

[4] D. Bushi, Y. Grad, S. Einav, O. Yodfat, B. Nishri, and D. Tanne, Hemodynamic evaluation of embolic trajectory in an arterial bifurcation: An *in vitro* experimental model, Stroke **36**, 2696 (2005).

[5] A. S. Kennedy, C. Kleinstreuer, C. A. Basciano, and W. A. Dezarn, Computer modeling of yttrium-90-Microsphere transport in the hepatic arterial tree to improve clinical outcomes, Intl. J. Radiat. Oncol. Biol. Phys. **76**, 631 (2010).

[6] A. L. Richards, C. Kleinstreuer, A. S. Kennedy, E. Childress, and G. D. Buckner, Experimental microsphere targeting in a representative hepatic artery system, IEEE Trans. Biomed. Eng. **59**, 198 (2011).

[7] C. A. Basciano, C. Kleinstreuer, A. S. Kennedy, W. A. Dezarn, and E. Childress, Computer modeling of controlled microsphere release and targeting in a representative hepatic artery system, Ann. Biomed. Eng. **38**, 1862 (2010).

[8] S. J. Zhu, E. K. Poon, A. S. Ooi, and S. Moore, Enhanced targeted drug delivery through controlled release in a three-dimensional vascular tree, J. Biomech. Eng. **137**, 031002 (2015).

[9] M. Caine, M. S. McCafferty, S. McGhee, P. Garcia, W. M. Mullett, X. Zhang, M. Hill, M. R. Dreher, and A. L. Lewis, Impact of yttrium-90 microsphere density, flow dynamics, and administration technique on spatial distribution: Analysis using an *in vitro* model, J. Vascular Intervent. Radiol. **28**, 260 (2017).

[10] I. A. Carr, N. Nemoto, R. S. Schwartz, and S. C. Shadden, Size-dependent predilections of cardiogenic embolic transport, Am. J. Physiol.: Heart Circ. Physiol. **305**, H732 (2013).

[11] D. Mukherjee, N. D. Jani, K. Selvaganesan, C. L. Weng, and S. C. Shadden, Computational assessment of the relation between embolism source and embolus distribution to the circle of willis for improved understanding of stroke etiology, J. Biomech. Eng. **138**, 081008 (2016).

[12] O. Amili, J. Golzarian, and F. Coletti, *In vitro* study of particle transport in successively bifurcating vessels, Ann. Biomed. Eng. **47**, 2271 (2019).

[13] R. Ditchfield and W. Olbricht, Effects of particle concentration on the partitioning of suspensions at small divergent bifurcations, J. Biomech. Eng. **118**, 287 (1996).

[14] H. Stauber, D. Waisman, N. Korin, and J. Sznitman, Red blood cell dynamics in biomimetic microfluidic networks of pulmonary alveolar capillaries, Biomicrofluidics **11**, 014103 (2017).

[15] E. R. Weibel, A. F. Cournand, and D. W. Richards, *Morphometry of the Human Lung* (Springer, New York, 1963), Vol. 1.

[16] J. Comer, C. Kleinstreuer, and Z. Zhang, Flow structures and particle deposition patterns in double-bifurcation airway models. Part 1. Air flow fields, J. Fluid Mech. **435**, 25 (2001).

[17] S. Jalal, A. Nemes, T. Van de Moortele, S. Schmitter, and F. Coletti, Three-dimensional inspiratory flow in a double bifurcation airway model, Expt. Fluids **57**, 148 (2016).

[18] X. Chen, Y. Feng, W. Zhong, B. Sun, and F. Tao, Numerical investigation of particle deposition in a triple bifurcation airway due to gravitational sedimentation and inertial impaction, Powder Technol. **323**, 284 (2018).

[19] C. T. Crowe, J. D. Schwarzkopf, M. Sommerfeld, and Y. Tsuji, *Multiphase Flows with Droplets and Particles* (CRC Press, Boca Raton, FL, 2011).

[20] N. T. Ouellette, H. Xu, and E. Bodenschatz, A quantitative study of three-dimensional Lagrangian particle tracking algorithms, Exp. Fluids **40**, 301 (2006).

[21] G. A. Voth, A. La Porta, A. M. Crawford, J. Alexander, and E. Bodenschatz, Measurement of particle accelerations in fully developed turbulence, J. Fluid Mech. **469**, 121 (2002).

[22] M. Ebrahimian, R. S. Sanders, and S. Ghaemi, Dynamics and wall collision of inertial particles in a solid-liquid turbulent channel flow, J. Fluid Mech. **881**, 872 (2019).

[23] L. J. Baker and F. Coletti, Particle-fluid-wall interaction of inertial spherical particles in a turbulent boundary layer, J. Fluid Mech. **908**, A39 (2021).

[24] J. S. Bendat and A. G. Piersol, *Random Data: Analysis and Measurement Procedures* (Wiley, New York, 2011), Vol. 729.

[25] F. Toschi and E. Bodenschatz, Lagrangian properties of particles in turbulence, Annu. Rev. Fluid Mech. **41**, 375 (2009).

[26] N. T. Ouellette, H. Xu, M. Bourgoin, and E. Bodenschatz, An experimental study of turbulent relative dispersion models, New J. Phys. **8**, 109 (2006).

[27] R. Kannan, P. Guo, and A. Przekwas, Particle transport in the human respiratory tract: Formulation of a nodal inverse distance weighted Eulerian-Lagrangian transport and implementation of the Wind-Kessel algorithm for an oral delivery, Intl. J. Numer. Methods Biomed. Eng. **32**, e02746 (2016).

[28] R. Kannan, R. Arey, A. Przekwas, A. Berlinski, and N. Singh, Evaluating drug deposition patterns from Turbuhaler® in healthy and diseased lung models of preschool children, J. Pulmon. Med. Resp. Care **4**, 1008 (2022).

[29] R. Salem and R. J. Lewandowski, Chemoembolization and radioembolization for hepatocellular carcinoma, Clin. Gastroenterol. Hepatol. **11**, 604 (2013).

[30] N. R. Crookston, G. S. Fung, and E. C. Frey, Development of a customizable hepatic arterial tree and particle transport model for use in treatment planning, IEEE Trans. Radiat. Plasma Med. Sci. **3**, 31 (2018).

[31] C. Kleinstreuer, Y. Feng, and E. Childress, Drug-targeting methodologies with applications: A review, WJCC **2**, 742 (2014).

[32] S. S. Meschi, A. Farghadan, and A. Arzani, Flow topology and targeted drug delivery in cardiovascular disease, J. Biomech. **119**, 110307 (2021).